Journal of Instrumentation

Assessment of MR-compatibility of SiPM PET insert using short optical fiber bundles for small animal research

To cite this article: H.G. Kang *et al* 2015 *JINST* **10** P12008

PUBLISHED BY IOP PUBLISHING FOR SISSA MEDIALAB
RECEIVED: *July 19, 2015*
REVISED: *September 30, 2015*
ACCEPTED: *November 11, 2015*
PUBLISHED: *December 11, 2015*

Assessment of MR-compatibility of SiPM PET insert using short optical fiber bundles for small animal research

H.G. Kang,[a] **S.J. Hong,**[a,b,1] **G.B. Ko,**[c] **H.S. Yoon,**[c] **I.C. Song,**[d] **J.T. Rhee**[e] **and J.S. Lee**[c]

[a]*Department of Senior Healthcare, Graduate School of Eulji University, 77 Mok-Dong, Seo-Gu, Daejeon, 301-746, Republic of Korea*
[b]*Department of Radiological Science, Eulji University, 553 Yangji-Dong, Sujeong-Gu, Seongnam-Si, Gyeonggi-Do, 431-713, Republic of Korea*
[c]*Departments of Nuclear Medicine and Biomedical Sciences, Seoul National University, 28 Yungun-Dong, Chongno-Gu, Seoul, 110-744, Republic of Korea*
[d]*Departments of Radiology, Seoul National University, 28 Yungun-Dong, Chongno-Gu, Seoul, 110-744, Republic of Korea*
[e]*Department of Physics, Konkuk University, 120 Hyayang-Dong, Gwangjin-Gu, Seoul, 143-701, Republic of Korea*

E-mail: hongseongj@eulji.ac.kr

ABSTRACT: Simultaneous positron emission tomography (PET) and magnetic resonance imaging (MRI) can provide new perspectives in human disease research because of their complementary in-vivo imaging techniques. Previously, we have developed an MR-compatible PET insert based on optical fibers using silicon photomultipliers (SiPM). However when echo planar imaging (EPI) sequence was performed, signal intensity was slowly decreased by −0.9% over the 5.5 minutes and significant geometrical distortion was observed as the PET insert was installed inside an MRI bore, indicating that the PET electronics and its shielding boxes might have been too close to an MR imaging object. In this paper, optical fiber bundles with a length of 54 mm instead of 31 mm were employed to minimize PET interference on MR images. Furthermore, the LYSO crystals with a size of $1.5 \times 1.5 \times 7.0\,\mathrm{mm}^3$ were used instead of $2.47 \times 2.74 \times 20.0\,\mathrm{mm}^3$ for preclinical PET/MR applications. To improve the MR image quality, two receive-only loop coils were used. The effects of the PET insert on the SNR of the MR image either for morphological or advanced MR pulse sequences such as diffusion weighted imaging (DWI), functional MRI (fMRI), and magnetic resonance spectroscopy (MRS) were investigated. The quantitative MR compatibility such as B_0 and B_1 field homogeneity without PET, with 'PET OFF', and with 'PET ON' was also evaluated. In conclusion, B_0 maps were not affected by the proposed PET insert whereas B_1 maps were significantly affected by the PET insert. The advanced MRI sequences such as DWI, EPI, and MRS can be performed without a significant MR image quality degradation.

KEYWORDS: Multi-modality systems; MRI (whole body, cardiovascular, breast, others), MR-angiography (MRA); Gamma camera, SPECT, PET PET/CT, coronary CT angiography (CTA)

[1]Corresponding author.

doi:10.1088/1748-0221/10/12/P12008

2015 JINST 10 P12008

Contents

2015 JINST 10 P12008

1 Introduction

An integrated PET/MR scanner has emerged as a new in-vivo molecular imaging modality as it can visualize both functional and anatomical information simultaneously. In particular, the use of magnetic resonance imaging (MRI) enables the PET/MR to be used for diagnosis in brain disease, and research in neurodegenerative disorder [1–4].

In the early stage of the development of simultaneous PET/MR modality, long optical fibers have played an important role of transferring scintillation photons to photomultiplier tubes (PMTs) in the fringe of magnetic field [5–8]. However, the axial field of view (FOV) of PET employing optical fiber bundles was restricted by the bending of the optical fiber bundle inside the MRI. With the advent of MR-compatible avalanche photodiodes (APDs), the simultaneous PET/MR imaging with a long axial FOV became possible, something which was difficult with the PET/MR system employing the long optical fibers and PMTs. The APD based PET/MR systems have shown promising results not only for preclinical research but also for clinical application [9]. The PET detector modules in a commercial whole-body PET/MR scanner, which is based on avalanche photodiodes (APDs), are positioned between the body radio-frequency (RF) coil and the gradient coil. Consequently, the MRI needed significant modifications which required an increased manufacturing cost [10].

Recently, silicon-photomultipliers (SiPMs) and digital SiPMs (dSiPMs) which have a comparable gain to the conventional PMT are used for the development of an MR-compatible PET insert [11–18]. Even though an MR-compatible PET insert is rarely used as a whole-body PET/MR scanner, due to space constraints inside the MRI bore, PET inserts are still attractive in the PET/MR scanners dedicated to brain or preclinical research.

Apart from the RF transparent PET detector [19], most MR-compatible PET inserts require either custom-made or existing RF transceiver coils for RF transmission and signal reception [2, 20] since RF excitation pulses transmitted by a body RF coil cannot penetrate the PET inserts, the electronics of which are enclosed with copper sheets to protect against MRI RF interferences [2]. Latest trends of MR imaging, particularly of parallel imaging, use the body coil for RF transmission and receive-only multi-channel coils for RF reception such that the RF excitation pulses can be transmitted uniformly throughout an imaging object and that RF reception sensitivity can be improved. Since the electronics and its copper shields out of the various components of the PET inserts deteriorate the homogeneity in MR magnetic field, it is important to keep them away from the imaging object. Advanced MR imaging techniques such as diffusion weighted imaging (DWI), echo planar imaging (EPI) and MR spectroscopy (MRS) can take advantage of the homogeneity in magnetic field. Even though dedicated RF transceiver coils for simultaneous PET/MRI are ideal, they are quite expensive and need extensive works to verify the compatibility with various MRIs produced by different manufacturers. Therefore, RF coils already verified to particular MRIs are highly beneficial to save both time and costs.

In the previous research, we demonstrated the feasibility of the MR-compatible SiPM-PET insert employing relatively short optical fiber bundles for simultaneous PET/MR imaging [13]. To explain briefly the previous research, the MR-compatible PET insert system (hereafter, the PET insert prototype) was comprised of 12 SiPM-PET modules, each of which had a 6×6 array of LYSO crystals with a dimension of $2.47 \times 2.74 \times 20.0\,\mathrm{mm}^3$, an optical fiber bundle with a length of 31 mm and a SiPM with 4×4 sensitive cells, each of which had an area of $3 \times 3\,\mathrm{mm}^2$. However even though optical fiber bundles with a 31 mm length were used, signal intensity was slowly decreased by -0.9% over the 5.5 minutes of EPI sequences. Significant geometrical distortion was also observed, indicating that the PET electronics and its shielding boxes might have been too close to an MR imaging object [14]. Based on the previous study, we have developed an MR-compatible SiPM PET insert (hereafter, the small animal PET insert) for simultaneous small animal PET/MR imaging. This small animal PET insert consisted of 12 SiPM-PET modules, each of which had 9×9 arrays of LYSO crystals with a dimension of $1.5 \times 1.5 \times 7.0\,\mathrm{mm}^3$, an optical fiber bundle with a length of 47 mm and the same SiPMs as in the previous study. The crystal length of 7.0 mm was selected to minimize the parallax effect at the periphery of transverse field-of-view. We had presented simultaneous PET/MR in-vivo mouse images with the small animal PET insert installed inside a 3 T MRI (MAGNETOM Trio, Siemens AG) at the 2012 Society of Nuclear Medicine and Molecular Imaging (SNMMI) annual meeting [21]. The previous small animal PET insert had too small a diameter to insert two or multiple receiver coils into the PET insert bore and too short an axial length severely limiting sensitivity. In this paper, we present an assessment of MR-compatibility of another SiPM PET insert (hereafter, the small animal large-bore PET insert) which had 32.7 mm in an axial FOV and 128 mm in a ring diameter. The detector module of the small animal large-bore PET insert consisted of 18×20 array of $1.5 \times 1.5 \times 7.0\,\mathrm{mm}^3$ LYSO crystals, 2×2 SiPM (Hamamatsu, S11064-050P) array, and a 54 mm long optical fiber bundle. Each SiPM has 4×4 sensitive channels, each of which has a sensitive area of $3 \times 3\,\mathrm{mm}^2$ and consists of 3,600 pixels with a size of $50 \times 50\,\mu\mathrm{m}^2$. MR performances of the small animal large-bore PET insert have been presented.

2 Materials and methods

2.1 Small animal PET insert

2.1.1 Small animal large-bore PET insert block detector

A LYSO crystal block in figure 1 consisted of an 18×20 array ($29.3 \times 32.7\,\mathrm{mm}^2$) of a $1.5 \times 1.5 \times 7.0\,\mathrm{mm}^3$ LYSO crystal. Each crystal in the PET block detector was optically isolated using a square lattice built with a 0.065 mm thick 3M-ESR polymer [22]. An array of 2×2 sixteen channel SiPMs was used to detect scintillation light produced by annihilation photon interaction with the LYSO crystal array. The optical fiber bundle between the LYSO crystal block and the 2×2 SiPM array consisting of 64 channels was assembled with 374 optical fibers each of which has 54 mm in length and 2 mm in diameter. A soft polyvinyl chloride (PVC) layer with a thickness of 1 mm was inserted between the optical fiber bundle and the SiPM array, and optical grease was also applied to both sides of the PVC.

To ensure a good optical coupling between the LYSO crystal and the optical fiber bundle, and between the optical fiber bundle and the SiPM array, custom-made acrylonitrile butadiene styrene (ABS) jigs were used. The jigs in figure 1(e) were constructed using a 3D printing techniques (3D system, Viper Si2 SLA, U.S.A.). Since the ABS-like material used in the jigs is semi-transparent, three layers of black tape were pasted to prevent external light from entering into the PET module as shown in figure 2(c).

2.1.2 Readout electronics for PET signal encoding

The front-end electronics consisted of a resistive charge division network (RCN) board and differential amplifiers (AD8132, Analog Devices, U.S.A.) as shown in figure 2(a), (b). The RCN reduced the 64 signals of the PET block detector module into 4 signals [23]. A ‘sum’ signal was generated by adding the 4 signals to trigger annihilation gamma events. The four signals represented as A, B, C, and D and the ‘sum’ signal were amplified by a factor of 10 with the differential amplifiers. The differential, instead of a single-ended, amplifiers were used to reduce RF noise interference. The ‘sum’ signal was amplified one more time by a differential receiving amplifier (AD8130, Analog Devices, U.S.A.) for better determination of timing. The read-out electronics were enclosed in a

2015 JINST 10 P12008

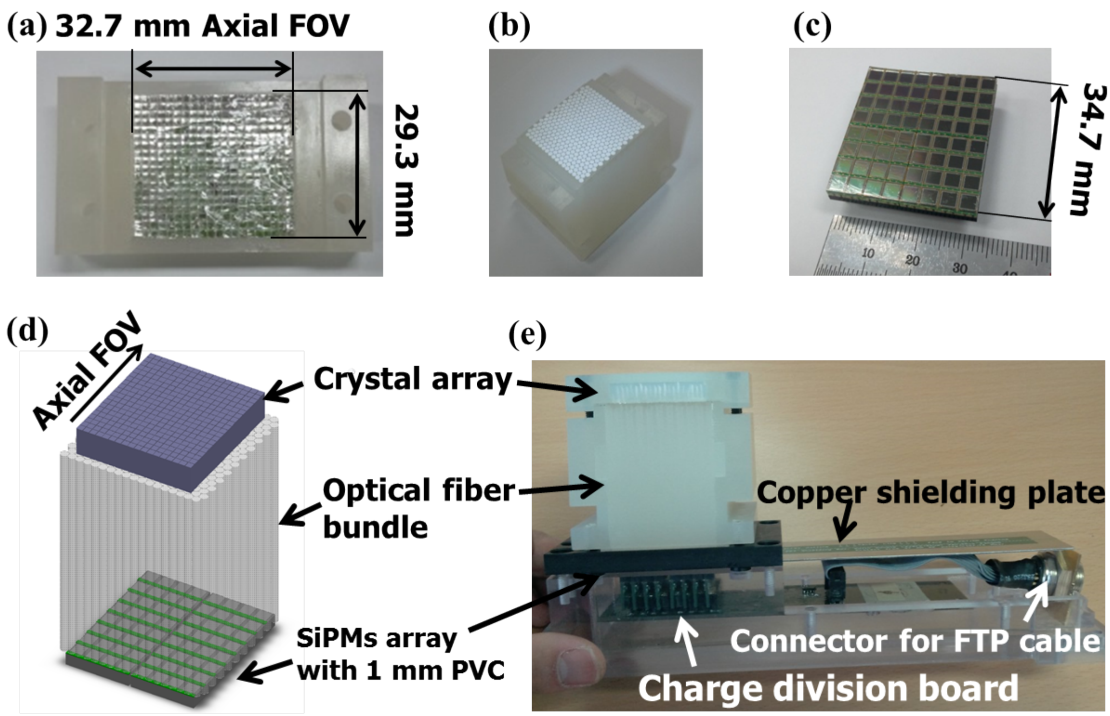

Figure 1. One of the PET insert modules: (a) PET block detector, (b) optical fiber bundle assembled in a custum made jig, (c) SiPM array of 2×2 consisting of 64 channels, (d) schematic of the PET insert module, and (e) PET insert module showing the copper shielding plate on the top side only. Note that the SiPM is outside the copper shielding plate [13].

double layer copper shielding box with a dimension of $34 \times 24 \times 180\,\mathrm{mm}^3$, and each of the layers had 18 μm in thickness to prevent RF interference on the PET electronics as shown in figure 2(e). The edges of the shielding box were covered by a 0.05 mm thick copper foil to prevent RF leakage into the PET electronics as shown in figure 2(e). The SiPMs were outside the copper shielding box [13] and the SiPM pins (128 pins per module which corresponds to 64 channels of $3 \times 3\,\mathrm{mm}^2$ sensitive cell) were connected to the non-magnetic connecters of the charge division board using the through-holes of the shielding box as shown in figure 2(c).

The performance of the copper shielded PET insert module shown in figure 2(e) was evaluated using a data acquisition system which consisted of nuclear instrumentation module (NIM, Wiener, Germany) and versa module eurocard (VME, Wiener, Germany) modules. Figure 3 shows a data flow diagram. The ‘sum’ signal was sent to the differential receiving amplifier (AD8130, Analog Devices, U.S.A.) and then to a leading edge discriminator (LED) for triggering of coincident events. The four signals A, B, C and D which contain energy and position information were fed to a fan-in fan-out module and then digitized by a charge-to-digital converter. The ‘sum’ signal was sent to the differential receiving amplifier and then to a KN241 (Kaizu Works, Japan) leading edge discriminator (LED), and a digital signal from the LED was fed to a KN470 (Kaizu Works, Japan) logic module. A digital signal from the logic module was sent to a GATE generator (Model 222, LeCroy, U.S.A.) to create a 700 ns wide signal which were sent to both a GATE signal for a charge-

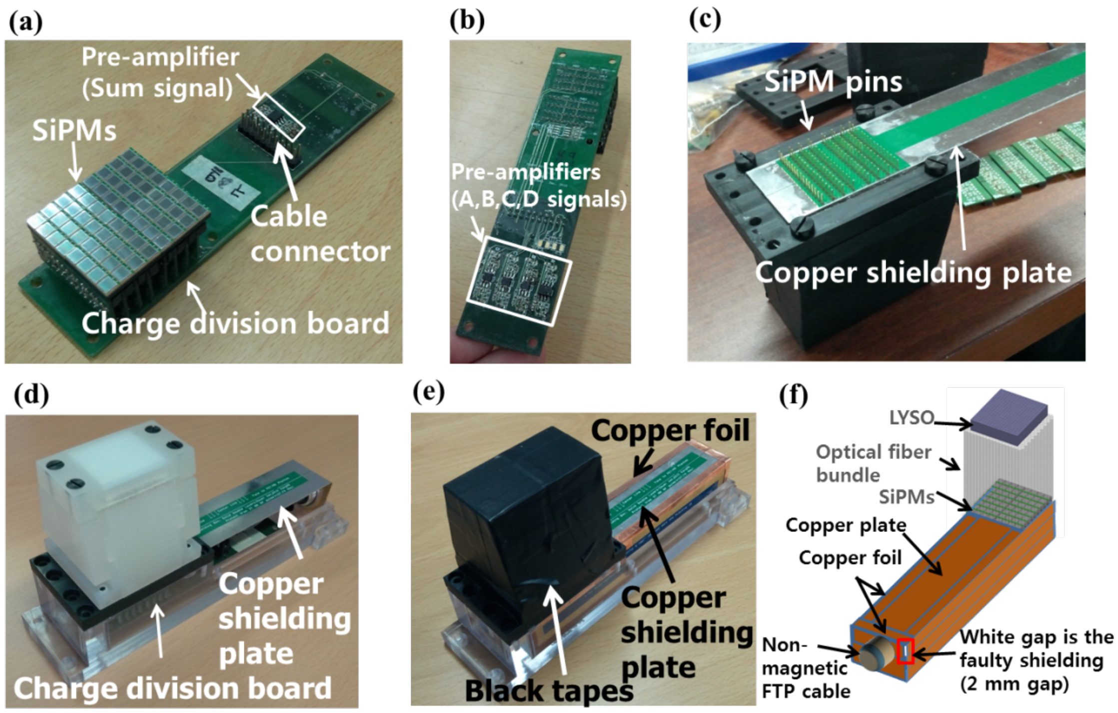

Figure 2. PET signal readout electronics and copper shielding: (a) SiPM and PET position encoding charge division board, (b) Differential amplifiers for position signals, (c) SiPM pins and through-holes of copper shielding plate, (d) SiPM PET module without complete copper shielding, (e) with complete copper shielding, and (f) faulty shielding in the edge of the shielding box with a 2 mm gap.

to-digital converter (QDC) module (CAEN, V965, Italy) and a STOP signal for a time-to-digital converter (TDC) module (CAEN, V775N, Italy).

Energy and coincidence timing resolutions, and crystal maps were obtained by placing a 3.7×10^5 Bq ^{22}Na point source between two PET insert modules. The room temperature was set to be 24°C using air conditioning.

2.1.3 Small animal large-bore PET insert configuration

The small animal PET insert presented at the 2012 SNM annual meeting had too small a diameter to insert two or multiple receiver coils into the PET insert bore and too short an axial length which limited sensitivity severely [21]. To solve these problems, a small animal large-bore PET insert in figure 4(a)–(c) was developed, which had 32.7 mm in an axial FOV and 128 mm in a ring diameter. The narrowest gap between the electronics boxes shielded with 2 layers of 18 μm thick copper sheets was 24 mm, and the distance between the electronics box and the center of FOV was 124 mm.

Figure 5 shows the schematic diagrams of the PET insert inside and outside an MRI room. The copper shielded 12 PET modules including the charge division network board were located inside the MRI bore. The high voltage for the SiPMs and the outputs signals of the differential amplifiers containing the crystal position information were transferred via 12 non-magnetic aluminum foil-screened twisted-pair cable (FTP) cables (Woori Electronics, Korea). The nonmagnetic connector

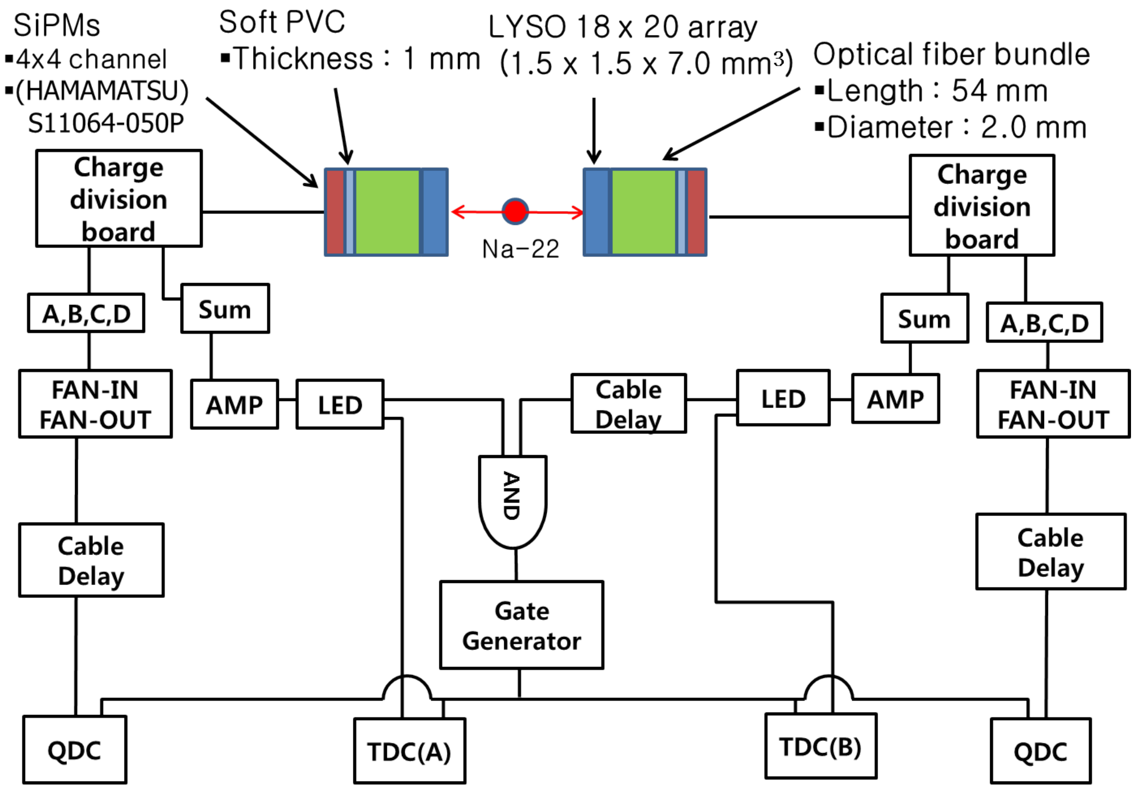

Figure 3. Data flow diagram to measure energy and coincidence timing resolutions of the small animal PET insert module.

(CONN 20POS, Woori Electronics, Korea) was used to connect the FTP cable to the charge division board as shown in figure 1(e). The 12 copper shielding boxes were grounded by an isolation metal panel on the wall of the MRI room to minimize eddy currents induced in the copper shielding box by MRI gradient fields. The ground of the PET readout electronics were transferred via the FTP cables to the power supplies located outside the MRI room as shown in figure 5. All PET electronics except the front-end electronics (RCN board, differential amplifiers transmitter) were outside the MRI room. A 3.7×10^5 Bq ^{22}Na point source was attached in the MR RF receiver loop coil and the PET raw signal was observed using an oscilloscope to check MR RF interferences to the PET electronics.

2.2 MR-compatibility of the PET insert

2.2.1 B_0 mapping with the small animal large-bore PET insert

To assess the effect of the PET insert on the main magnetic field homogeneity, a variation in the local magnetic field was measured using a cylindrical uniform gelatin phantom. The phantom with 4 cm in diameter and 6 cm in length was placed at the center of the PET insert FOV, and the PET insert was put at the center of the clinical 3 T MRI (MAGNETOM Trio, Siemens AG). The two RF receive loop coils, each of which has an inner coil diameter of 40 mm, were placed at the bottom and top of the cylindrical uniform gelatin phantom. An automatic shimming procedure was performed before the acquisition of B_0 map. Two phase images $\Phi(r,TE_1)$, $\Phi(r,TE_2)$ in the axial and

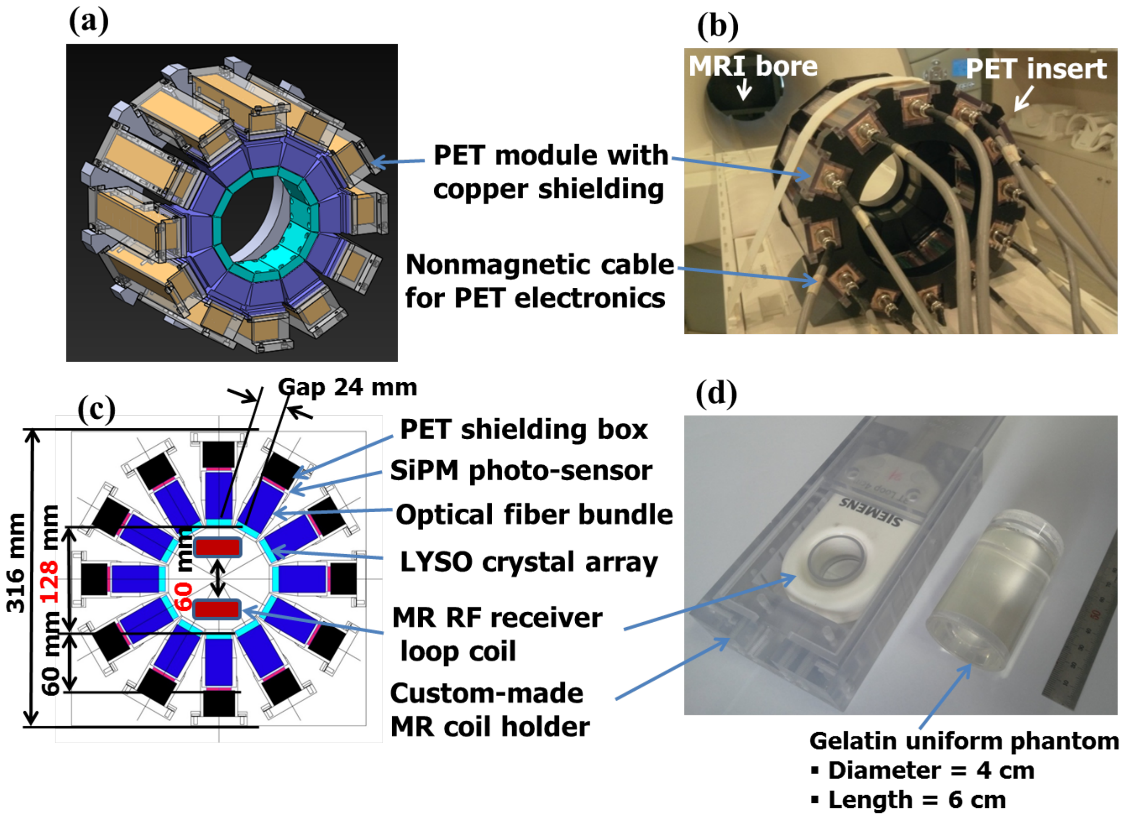

Figure 4. (a) 3D design view of the small animal large-bore PET insert, (b) photograph of the small animal large-bore PET insert, (c) schematic of the small animal large-bore PET insert with the dual receiver coils and with dual receiver coils, (d) the custom made MR coil holder and the gelatin uniform phantom.

coronal slices were obtained with a gradient echo sequence (TR = 500 ms, TE_1 = 10 ms and TE_2 = 20 ms, slice thickness = 2 mm, flip angle = 720°) [24]. Two phase images were reconstructed from raw MRI data using the inverse Fourier transform in Matlab (Mathworks, U.S.A.). Subsequently the local magnetic field map was calculated using a phase unwrapping algorithm [25], with the following eq. (2.1) [3, 26].

$$\Delta B_0(r) = \frac{\Phi\left(r, \mathrm{TE}_2\right) - \Phi\left(r, \mathrm{TE}_1\right)}{\gamma(\mathrm{TE}_2 - \mathrm{TE}_1)} \tag{2.1}$$

where, γ is the gyromagnetic ratio.

A binary mask image was obtained by applying the SNR threshold of 12 to the magnitude image. The binary mask image was used to generate the B_0 map which represented only the region of the cylindrical uniform gelatin phantom.

2.2.2 B_1 mapping with the small animal large-bore PET insert

To investigate the effect of the PET insert on the flip angle distribution homogeneity, RF field maps were measured with a cylindrical uniform gelatin phantom used in the B_0 mapping. The B_1 maps were obtained by using an RF field mapping sequence (TR = 300 ms, TE = 17 ms, slice thickness = 10 mm, flip angle = 720°) which employed a 90° RF pulse and two refocusing pulses

2015 JINST 10 P12008

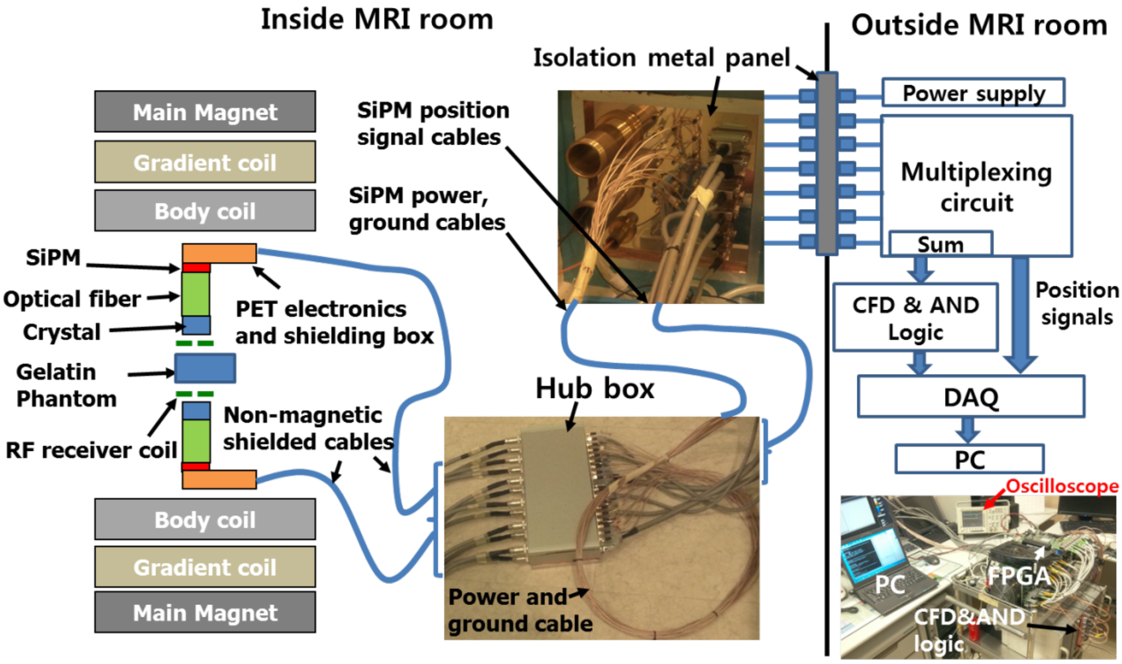

Figure 5. Schematic diagrams of the PET insert inside and outside MRI room.

to acquire the conventional spin-echo (SE) and stimulated-echo (STE) sequence produced by three RF pulses [3, 27–29]. The B_1 maps were exported as a digital imaging and communications in medicine (DICOM) format and analyzed using the Matlab. The following eq. (2.2) was used to calculate the flip angle α distribution [3].

$$\alpha \approx \arccos\left(\frac{\mathrm{SI_{STE}}}{\mathrm{SI_{SE}}}\right) \tag{2.2}$$

2.2.3 Feasibility of MRI, fMRI, and MR spectroscopy with the small animal large-bore PET insert

The feasibility of the small animal large-bore PET insert for MRI, fMRI and MR spectroscopy was investigated inside the clinical 3 T MRI. The body coil transmitted RF and two RF receiver loop coils received RF signals. For reproducible and stable loop coil positioning, a custom made MR receiver coil holder in figure 4(d) was used.

A cylindrical gelatin uniform phantom with 40 mm in diameter and 60 mm in length was used, which was placed at the center of PET insert FOV, and the PET insert was put at the center of the clinical 3 T MRI. A 3.7×10^5 Bq ^{22}Na point source was attached to the bottom of the cylindrical gelatin uniform phantom to measure the PET signal during the MR operation. The signal to noise ratio (SNR) of MR images with and without the small animal large-bore PET insert was investigated with the gelatin phantom using various MR pulse sequences such as T2-TSE, 3D-SPGR, diffusion weighted imaging (DWI) and diffusion tensor imaging (DTI) shown in table 1. The SNR was calculated using eq. (2.3).

$$\mathrm{SNR} = 0.655\frac{S_{\mathrm{ROI}}}{\sigma_{\mathrm{bkg}}} \tag{2.3}$$

Table 1. MR pulse sequences parameters.

Pulse sequence	TR [ms]	TE [ms]	TI [ms]	α [°]	Number of averages	ΔZ [mm]	Bandwidth [Hz/pixel]
T2-TSE	3,000	97	–	120	4	3	196
3D-SPGR	1,670	2.71	900	9	1	1	271
DWI	2,100	75.5	–	180	8	4	992
DTI	9,100	92	–	90	1	4	1,698

where, the S_{ROI} is the mean pixel value of the ROI with a 60% area of the uniform gelatin phantom and σ_{bkg} is the standard deviation of the background pixels outside the uniform gelatin phantom with an area of 1 cm^2 as shown in figure 13(a) [26].

To investigate the feasibility of simultaneous PET/fMRI imaging, EPI image quality was evaluated according to protocol recommended by Function Biomedical Informatics Research Network (FBIRN) [30]. For MR signal detection, two RF receiver coils with a 40 mm inner diameter were used as shown in figure 4(c) and (d). A gradient-recalled EPI sequence was employed (TR = 2,000 ms, TE = 30 ms, flip angle = 90, FOV 64 × 64 mm^2, slice thickness = 2.0 mm, 10 slices, the number of phase encoding steps = 64, pixel bandwidth = 2,298 Hz/pixel) and total 200 volume scans (one volume contains all slices measured per scan) were obtained per experimental run which lasted for 6 min 44 sec. Even though the acquisition time for one volume scan (image) was 1.04 sec, 200 images were taken over the 6 min 44 sec and each volume scan consisted of 10 slices [31].

To assess the quality of MRS in the presence of PET insert, isopropyl alcohol (C_3H_7OH) of 17 ml was placed in the center of the PET/MR FOV and single-voxel proton spectroscopy was conducted. The isotropic voxel of 20 × 20 × 20 mm^3 was selected and a point resolved spectroscopy (PRESS) pulse sequence was performed. To ensure the magnetic field homogeneity across the MRS syringe phantom, automatic instead of manual shimming was performed as clinical MRS examination requires the automated shimming procedure. The MRS data was analyzed using a jMRUI software package (version 5) [32]. Post-processing procedures such as zero filling, apodization using Gaussian window (sigma = 40 Hz), phase correction and baseline correction were also applied. The MRS data were taken with and without the PET insert for comparison.

3 Results

3.1 Small animal PET insert

3.1.1 Performance of the small animal large-bore PET block detector

Figure 6(a) shows a crystal map and the line profiles of the row and column marked by white dotted rectangles the small animal large-bore PET insert detector module. Figure 6(b) shows QDC distributions with energy resolutions of 19.7%, 21.1%, and 25.5% at the center, middle, and edge from the crystals marked by red squares in the crystal map, respectively. Figure 6(c) shows the TDC distributions of the same crystals marked by red squares with coincidence time resolution of 17 ns, 16 ns, and 19 ns respectively. The average energy resolution and coincidence time resolution over the crystal map in figure 6 were 22.3 ± 6.2% and 18 ± 4 ns respectively. Even though individual

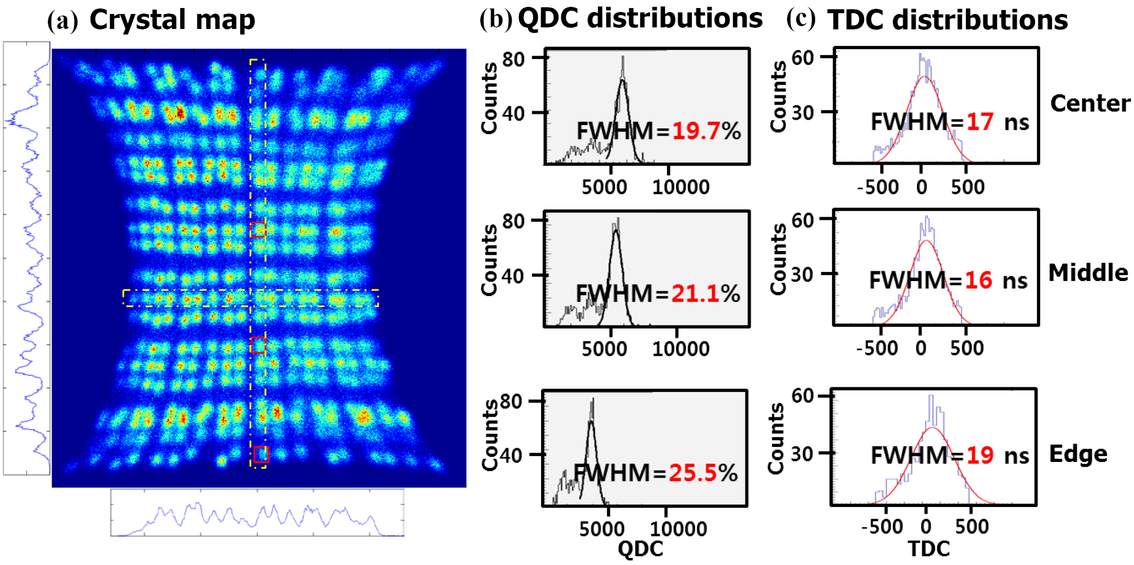

Figure 6. Test results from a small animal large-bore PET insert module: (a) the crystal map, (b) the QDC distributions, and (c) TDC distributions.

crystals in the middle rows of the crystal map were distinguishable, some crystals at the top and bottom rows were not clearly identified and some were merged together.

3.2 MR-compatibility of the PET insert

3.2.1 B_0 map distortion with the small animal large-bore PET insert

The local magnetic field variations in the axial and coronal slices for without PET, with 'PET OFF', with 'PET ON' were shown in figure 7 and 8. The circumferential region of the axial slice in figure 7 was distorted because of the magnetic susceptibility effect caused by the air and phantom interface. This magnetic susceptibility artifact was also found in the front and back regions of the phantom which correspond to the top and bottom region of the B_0 map image, as shown in the figure 8.

The maximum ΔB_0 differences in the 60% cross sectional area, marked by the white circle in figure 7, of the cylindrical gelatin uniform phantom in the axial slices were 2.5 μT, 2.8 μT and 2.6 μT for without PET, with 'PET OFF', and with 'PET ON' respectively. The maximum ΔB_0 difference of 2.6 μT with 'PET ON' in axial slice can be converted into 0.9 ppm with respect to the main magnetic field strength of 2.89 T, which was calculated from the Larmor frequency of 123.23 MHz transmitted into the phantom. The B_0 field inhomogeneity of 0.9 ppm is less than 1.0 ppm, which is required by the manufacturer's specification.

The maximum ΔB_0 differences throughout the PET axial FOV in the coronal slices within the 60% cross sectional area, represented by the white square in figure 8, of the cylindrical gelatin uniform phantom were 4.2 μT, 5.1 μT and 4.8 μT for without PET, with 'PET OFF', and with 'PET ON' respectively.

The maximum ΔB_0 difference in the coronal slices between with 'PET ON' and without PET in figure 8 was 0.6 μT (0.21 ppm), which is within the magnetic field drift criteria of 1.0 ppm per day recommend by the American Association of Physicists in Medicine (AAPM).

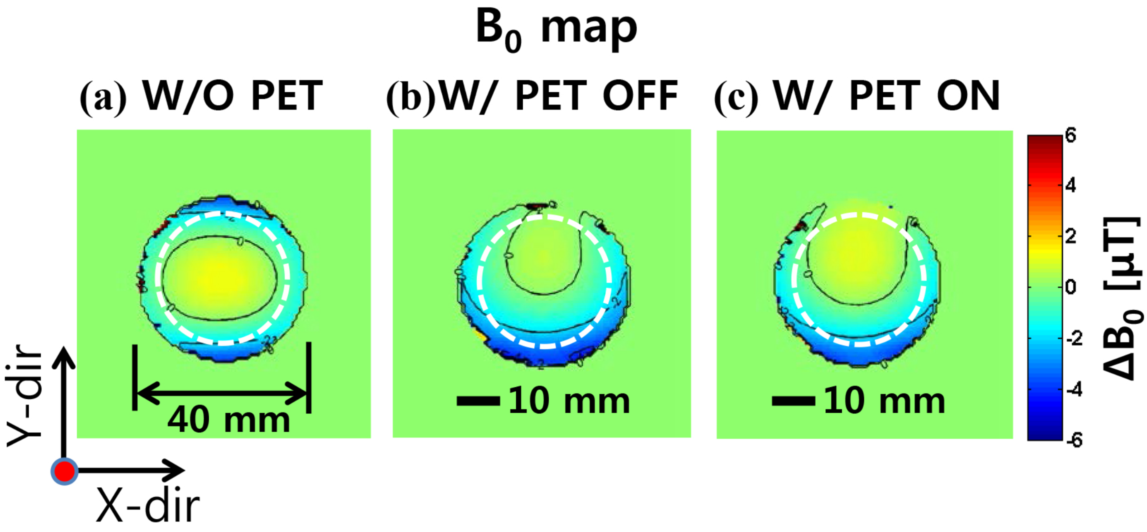

Figure 7. B_0 field maps in the axial slice: (a) without, PET (b) with 'PET OFF', and (c) with 'PET ON'.

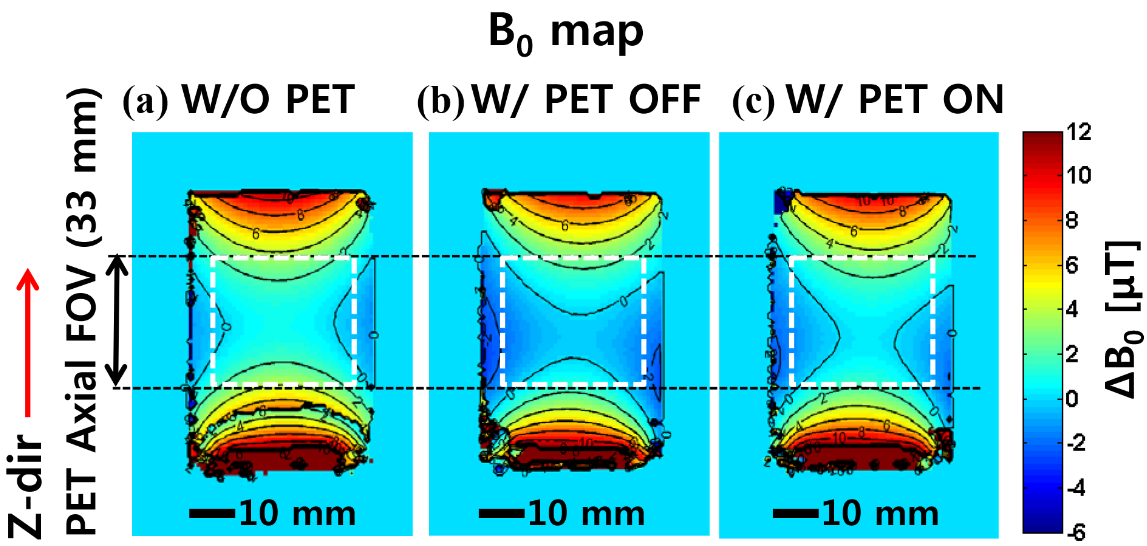

Figure 8. B_0 field maps in the coronal slice: (a) without, PET (b) with 'PET OFF', and (c) with 'PET ON'.

3.2.2 B_1 map distortion with the small animal large-bore PET insert

The RF field maps in the axial and coronal orientation were significantly affected by the PET as shown in figure 9 and 10. This was mainly because the excitation RF pulses produced by the body coil were blocked by the shielding boxes of the PET insert while the excitation RF pulses were transmitted toward the cylindrical gelatin uniform phantom. The maximum and minimum flip angles in axial orientation without PET, with 'PET OFF', and with 'PET ON' were 85°, 62°, 67° and 29°, 9°, 13° in the 60% cross sectional area respectively. The maximum and minimum flip angles in coronal orientation without PET, with 'PET OFF', and with 'PET ON' were 94°, 83°, 85° and 30°, 5°, 8° in the 60% cross sectional area respectively.

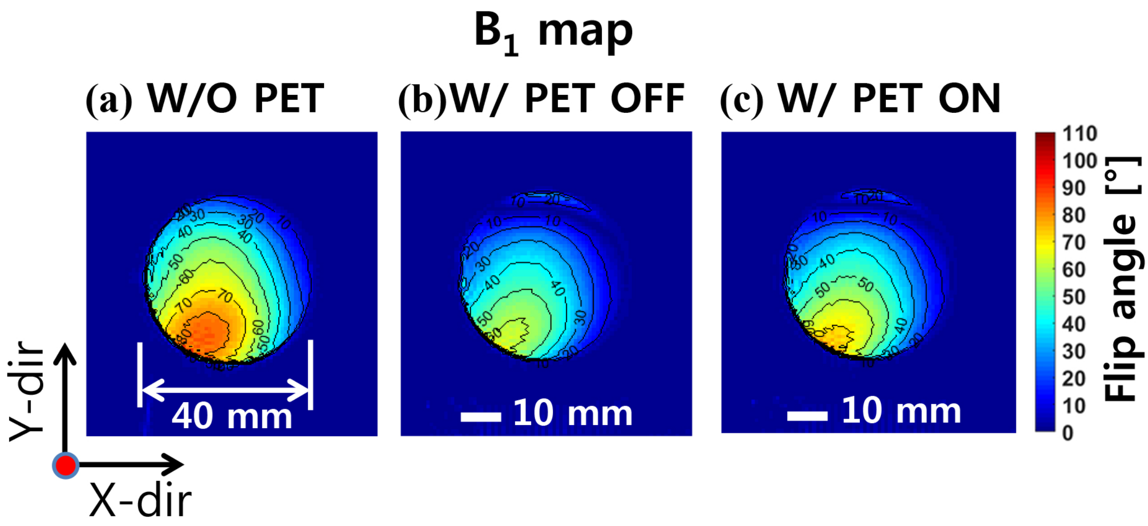

Figure 9. B_1 field maps in the axial slice: (a) without PET (b) with 'PET OFF', and (c) with 'PET ON'.

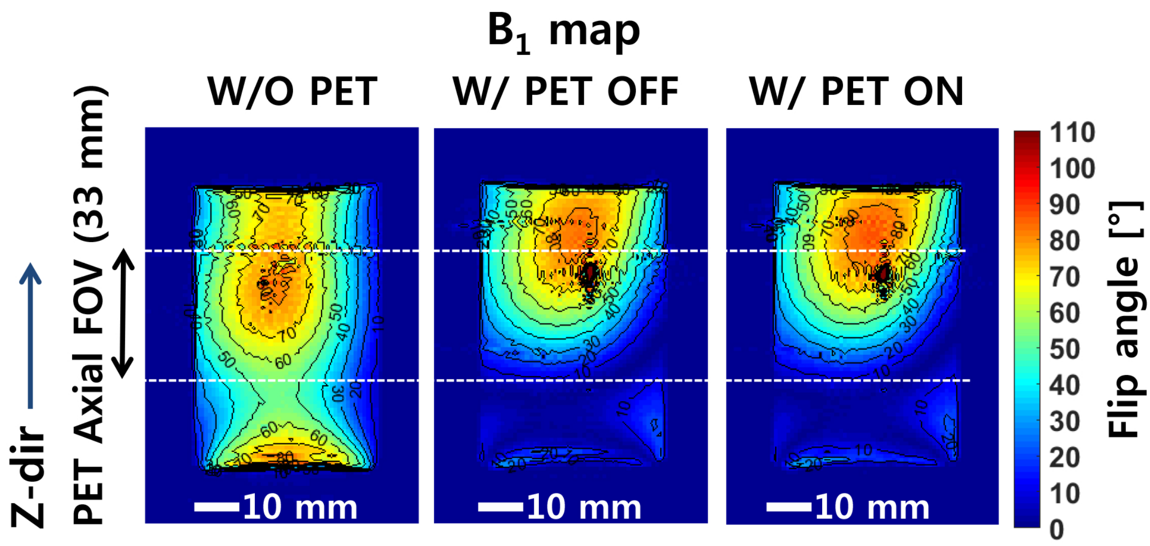

Figure 10. B_1 field maps in the coronal slice: (a) without PET (b) with 'PET OFF', and (c) with 'PET ON'.

3.2.3 Effect of the number of the MR receiver coils on MR image quality

As the number of MR receiver coils increased from one to two, the uniformity of MR signal intensity over the longitudinal direction was significantly improved in the T2-TSE pulse sequence as shown in figure 11. Figure 11 also shows signal intensities over the vertical lines represented by the dashed lines.

3.2.4 PET shielding effect on MR image quality

As shown in figure 12, the signals from the small animal large-bore PET did not contain MR RF interference noises when proper RF shielding was done. On the contrary, significant MR RF noises appeared on the PET signals with faulty shielding of PET electronics such as gap and crack in the

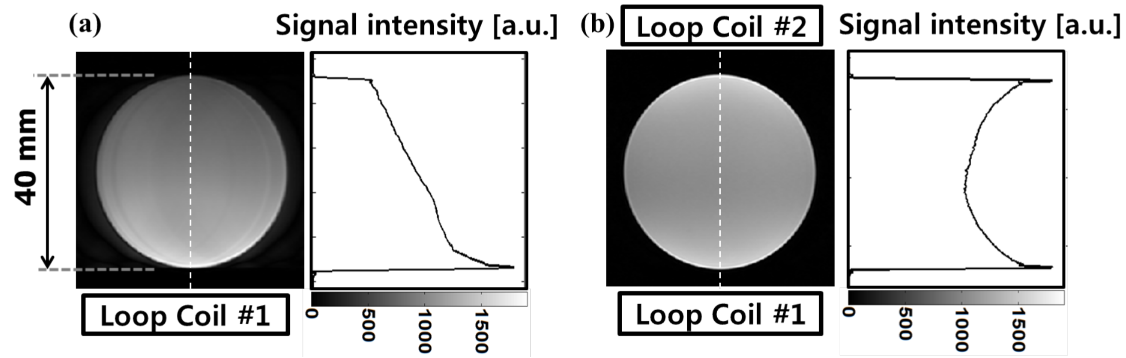

Figure 11. Comparison of the MR images and the signal intensities of the gelatin phantom using (a) a single receiver coil and (b) two receiver coils.

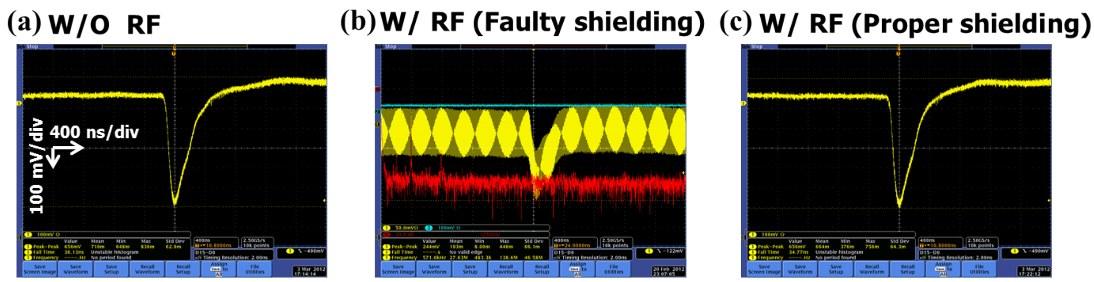

Figure 12. PET signals viewed from an oscilloscope: (a) without RF, (b) with faulty RF shielding, and (c) with proper RF shielding during MR operation.

copper shielding layer as shown in figure 2(f). These MR RF noises resulted in false triggering of coincidence detection in PET. The faulty shielding created by chance was the 2 mm gap between the copper plates covered by the copper foil and it resulted in RF interference on the PET signals observed with an oscilloscope.

The faulty shielding of PET electronics degraded MR image quality. The signal intensity was decreased by a factor of 2 while the SNR was decreased by about 40% from 257 ± 30 to 150 ± 16 as shown in figure 13. The measurement of MR image was repeated three times for each configuration (without PET, with 'PET OFF', and with 'PET ON'). The signal intensity for each configuration was within statistical limit when sufficient shielding was done, but the signal intensity with 'PET ON' was dropped significantly with the faulty shielding.

3.2.5 MR image quality with the small animal large-bore PET insert

Figure 14 shows T2-TSE, 3D-SPGR, DWI and DTI images without PET and with 'PET ON'. The p-values of the Student t-test between without PET and with 'PET ON' were 0.850 and 0.457 for the T2-TSE and DWI SNR averaged over 3 measurements respectively. In case of advanced MR pulse sequences like DWI and DTI which demand extremely uniform magnetic field homogeneity, slight changes in the shape of the gelatin phantom at the top and bottom region were observed due to the eddy current induced on the RF receiver coils by the diffusion gradient fields [33, 34].

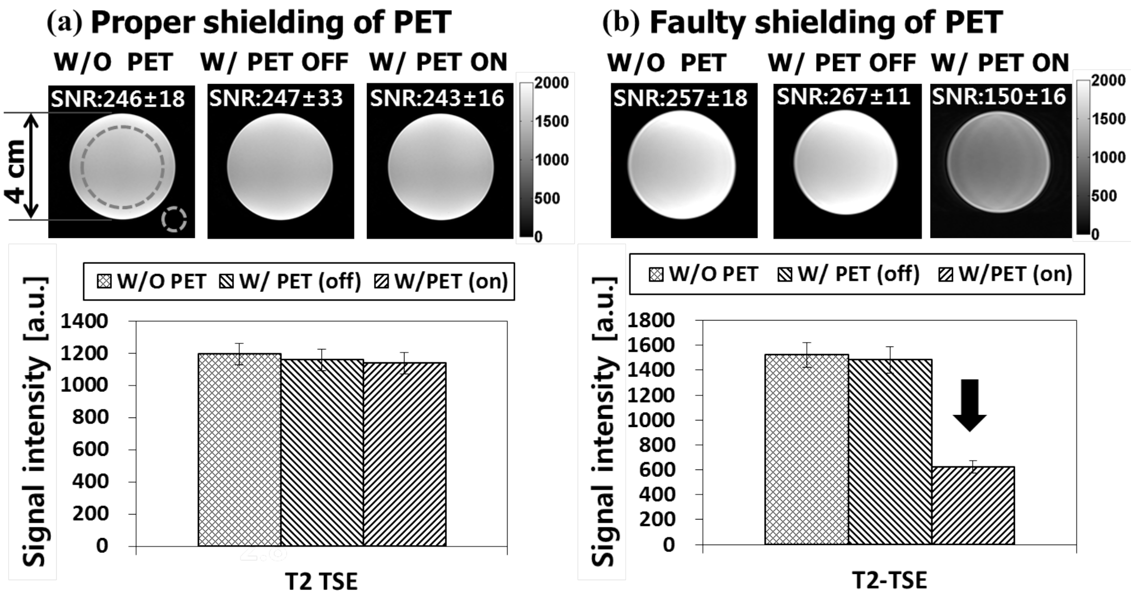

Figure 13. PET shielding effect on MR image quality (a) with proper shielding, and (b) with faulty shielding which refers to a 2 mm gap in the corner of the copper shielding box. Error bars indicate the standard deviations of 3 measurements.

Since the uniform gelatin phantom was used, all the images were supposed to be uniform regardless of without PET and with 'PET ON.' However, the DWI and DTI pulse sequences which evaluate the apparent diffusion of molecules normally produces less uniform images than the T2-TSE and 3D-SPGR pulse sequences because the DWI and DTI sequences were very sensitive to the Bo field inhomogeneity.

3.2.6 EPI image quality with the small animal large-bore PET insert

To investigate the temporal stability of EPI, we measured the signal intensity of EPI images with and without PET insert over the 6 min and 44 sec of the EPI sequence. The blue squares containing 49 pixels were used to calculate the mean signal intensities of EPI images. There was no significant spatial distortion in the shape of the gelatin phantom caused by the presence of small animal large-bore PET insert and during the PET operation as shown in figure 15(c) and (e). The small animal large-bore PET insert operation resulted in the 0.28% signal intensity drift as shown in figure 15(f).

3.2.7 MR spectroscopy with the small animal PET insert for dual receiver coils

The MR spectroscopy quality was evaluated with the small animal large-bore PET insert and there was no significant change in the peak positions and the full widths at half maximum (FWHM) as shown in figure 16. However the amplitudes of the three peaks were decreased by an average of 25% compared to the absence of the PET insert as shown in table 2, and the decrease was mainly due to the low transmission of RF excitation pulses to the metabolite object.

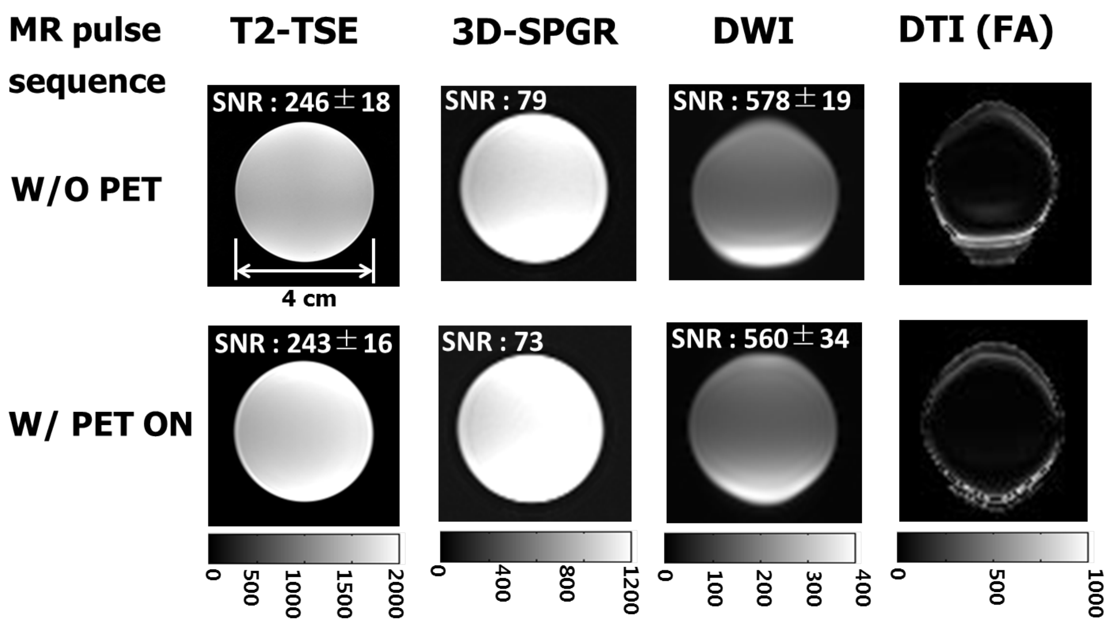

Figure 14. Comparison of MR image quality with and without small animal large-bore PET insert: (a) T2-TSE, (b) 3D-SPGR, (c) DWI, and (d) DTI sequences. (FA refers to the fractional anisotropy which represents the extent of the diffusion of the proton in water molecule).

Table 2. MR Spectroscopy results with and without the small animal large-bore PET insert.

	W/O PET			W/PET ON		
# of peak	Center [ppm]	FWHM [ppm]	Amplitude [a.u.]	Center [ppm]	FWHM [ppm]	Amplitude [a.u.]
1	1.56	0.36	1.22×10^{8}	1.55	0.35	9.27×10^{7}
2	4.36	0.34	1.18×10^{7}	4.35	0.33	9.26×10^{6}
3	5.85	0.32	2.06×10^{7}	5.83	0.30	1.38×10^{7}

4 Discussion

The proposed MR-compatible PET insert system is to be built with a short optical fiber bundle with a length of 30 mm ~ 100 mm such that degradation of timing and energy can be minimized unlike the MR-compatible PET scanner using PMTs with 4 m long optical fibers [6]. The proposed MR-compatible PET insert system can be installed with the existing commercial MRI without significant intrusion of the MR hardware whereas some traditional optical fiber based PET/MR approaches need modified MRI scanner [8]. One of the advantages of this MR-compatible PET system design is the extendibility of the axial and radial FOV unlike the design with the 90° bend of the optical fiber bundle [9].

The MR magnetic field homogeneity could be maintained because the optical fiber bundle enabled the PET electronics and its copper shielding box to be placed far away from the MR imaging object. A custom-built MR transceiver coil was not necessary because the body coil

2015 JINST 10 P12008

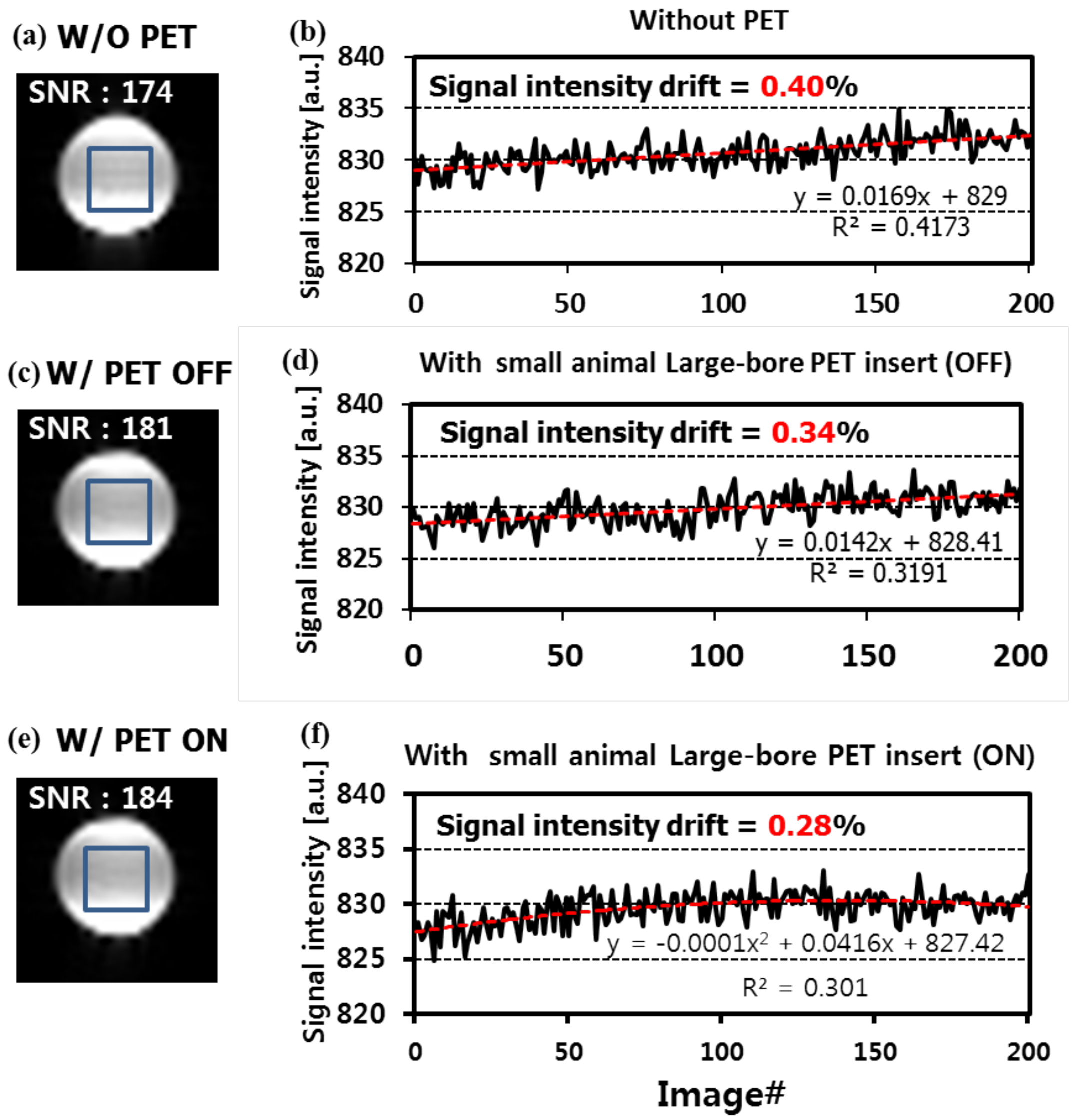

Figure 15. EPI signal intensity drifts: (a) and (b) without PET, (c) and (d) with 'PET OFF', and (e) and (f) with 'PET ON'.

transmitted the RF excitation pulse through the gap between PET block detector modules created by the use of the optical fiber bundle. PET/MR imaging thus can be obtained without much effort to develop a new custom-built MR local transceiver coil. This design concept which uses the body coil as a transmitter and the receiver-only coil as a RF signal receiver could also be beneficial for massively parallel MR imaging which needs the receiver as simple as possible [35, 36]. One of the main drawbacks of the proposed PET insert is the light loss of 40% caused by the use of optical fiber bundle. This leads to degradation in the energy and time resolution.

All the individual crystals of the crystal map in figure 6 were not clearly distinguishable because of the small crystal size of $1.5 \times 1.5 \times 7.0\,\mathrm{mm}^3$ and the relatively large fiber diameter of 2 mm. In our previous research, the detector block which resulted in clear separation between crystals consisted of the crystal size of $2.47 \times 2.74 \times 20\,\mathrm{mm}^3$ and the fiber diameter of 1 mm [13].

2015 JINST 10 P12008

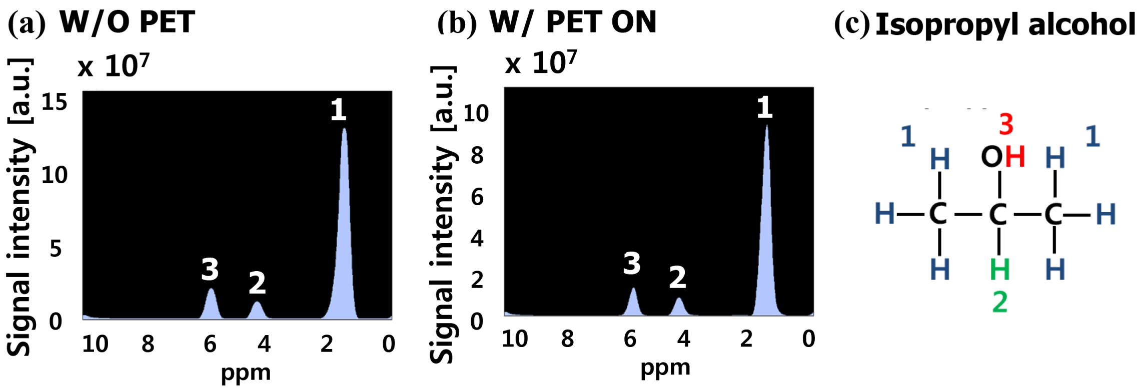

Figure 16. Spectra results of MR spectroscopy, (a) without PET, (b) with PET, (c) molecular structure of isopropyl alcohol with the indices for the individual spectroscopic peaks.

The number of SiPM signals in this study was increased by a factor of 4 than that in the previous study [13]. Increased number of the SiPM signals which were connected to resistive charge division network decreased the spacing between each pixel position in the flood map. The reduced spacing made the crystal decoding performance more vulnerable to noises. The smaller scintillation crystals in this study reduced the number of scintillation photons arriving to the photo-sensors compared to those in previous study [13]. Therefore, side resistors of 100 Ω instead of 10 Ω in the resistive charge division network had to be chosen to yield a wider dynamic range [23]. They improved the crystal decoding performance, but degraded spatial linearity to introduce the pin cushion distortion in figure 6.

The 'PET ON' test setup in the coronal slice of figure 8 resulted in a better main magnetic field homogeneity in field map compared to the test setups without PET and with 'PET OFF'. One of the reasons may be attributed to shimming conditions and MR slice positioning differences between test setups.

The maximum flip angle in the cylindrical gelatin phantom in an axial orientation was decreased from 88° to 67° when the PET insert was installed inside the MRI bore. The blocking of the RF excitation pulses, due to the copper shielding boxes of the PET insert block, caused the decrease. In addition the B_1 field homogeneity was also significantly deteriorated through the gelatin phantom, which was partly due to the phantom positioning differences between test setups. A careful measurement and evaluation of RF flip angle distribution without and with PET insert will be studied in the next study [37, 38].

Even though the single receiver coil which resulted in less uniformity can still be useful for a small FOV with less than 2 cm in diameter the MR image homogeneity obtained with the dual receiver coils is highly desirable for a larger FOV.

The proper copper shielding of PET electronics is an important factor which affects to the SNR of the MR image. Since the radiofrequency noises in the PET electronics interfered with the MR receiver coil, the noise of the MR image was increased. As a result, the SNR of the MR image with the faulty shielding was degraded by $\sim 60\%$ compared to the proper copper shielding of the PET electronics.

2015 JINST 10 P12008

The morphological MR imaging sequences such as T1w-TSE, T2w-TSE, 3D-SPGR were possible with the small animal PET insert without significant deterioration on MR image quality. However MR image qualities in advanced MR imaging techniques like EPI and DWI, were slightly distorted mainly due to magnetic field inhomogeneity caused by the small animal PET insert. MR operation did not deteriorate the performances of the small animal PET insert during various MR pulse sequences.

The drift in the signal intensity in figure 15(f) linearly increased up to the image number of $\sim$ 100, then it stabilized. Even a quadratic fit to the data gives a higher R^2 than a linear fit, the stabilization does not have physical bases and it appeared to be statistical fluctuations.

The small animal large-bore PET insert has shown the feasibility of simultaneous fMRI, MR spectroscopy and PET imaging with dual coils which lead to uniform signal intensity. Particularly the fMRI which visualizes the blood oxygen level dependent (BOLD) effect in the brain can complement the PET with a temporal resolution of 2 $\sim$ 3 sec since even brain dedicated PET has temporal resolution of several minutes [39, 40].

The PET insert prototype using the 31 mm long optical fiber bundles resulted in the decrease of EPI signal intensity by 0.9%, but the small animal large-bore PET insert using the 54 mm long optical fiber bundles resulted in the drift of EPI signal intensity by 0.34%. This smaller shift in the signal intensity was probably because the PET electronics were placed away from the imaging object. The small 0.34% drift of signal intensity indicates that the simultaneous PET/fMRI imaging is possible with the proposed small animal large-bore PET insert, since the typical change of signal intensity caused by BOLD effect is 2 $\sim$ 10% in a 3 T MRI [39, 41].

5 Conclusion

The MR-compatible PET inserts employing SiPMs and short optical fiber bundles have been developed and they produced encouraging results of simultaneous PET/MR imaging with effortless integration into the Siemens 3 T clinical MRI system. The use of existing and already verified receiver coils lead to the effortless integration.

The small animal PET inserts using short optical fiber bundle have demonstrated the feasibility of simultaneous PET/MR imaging for small animal without intrusion of the MRI. The small animal large-bore PET insert has shown the potential of fMRI and MR spectroscopy with simultaneous PET data acquisition. The crystal map obtained with the small crystal size and the large fiber diameter was not completely satisfactory. After improving the crystal map with a smaller fiber diameter, we plan to construct and evaluate another MR-compatible PET insert module.

Acknowledgments

This work was supported by grants from the Korean Research Foundation funded by the Korean Government (2010-001293).

References

[1] M.S. Judenhofer et al., *Simultaneous PET-MRI: a new approach for functional and morphological imaging*, *Nat. Med.* **14** (2008) 459.

[2] S.H. Maramraju et al., *Small animal simultaneous PET/MRI: initial experiences in a 9.4 T microMRI*, *Phys. Med. Biol.* **56** (2011) 2459.

[3] A. Kolb et al., *Technical performance evaluation of a human brain PET/MRI system*, *Eur. Radiol.* **22** (2012) 1776.

[4] H.F. Wehrl et al., *Pre-clinical PET/MR: technological advances and new perspectives in biomedical research*, *Eur. J. Nucl. Med. Mol. Imag.* **36 Suppl 1** (2009) S56.

[5] P.B. Garlick et al., *PET and NMR dual acquisition (PANDA): applications to isolated, perfused rat hearts*, *NMR Biomed.* **10** (1997) 138.

[6] Y. Shao et al., *Development of a PET detector system compatible with MRI/NMR systems*, *IEEE Trans. Nucl. Sci.* **44** (1997) 1167.

[7] S. Yiping et al., *Simultaneous PET and MR imaging*, *Phys. Med. Biol.* **42** (1997) 1965.

[8] A.J. Lucas et al., *Development of a combined microPET®-MR system*, *IEEE Trans. Nucl. Sci. Symp. Rec.* **4** (2006) 2345.

[9] H.-P.W. Schlemmer et al., *Simultaneous MR-PET Imaging of the Human Brain_Feasibility Study*, *Radiology* **248** (2008) 8.

[10] G. Delso et al., *Performance measurements of the Siemens mMR integrated whole-body PET/MR scanner*, *J. Nucl. Med.* **52** (2011) 1914.

[11] S.I. Kwon et al., *Development of small-animal PET prototype using silicon photomultiplier (SiPM): initial results of phantom and animal imaging studies*, *J. Nucl. Med.* **52** (2011) 572.

[12] H.S. Yoon et al., *Initial results of simultaneous PET/MRI experiments with an MRI-compatible silicon photomultiplier PET scanner*, *J. Nucl. Med.* **53** (2012) 608.

[13] S.J. Hong et al., *SiPM-PET with a short optical fiber bundle for simultaneous PET-MR imaging*, *Phys. Med. Biol.* **57** (2012) 3869.

[14] S. Yamamoto et al., *Interference between PET and MRI sub-systems in a silicon-photomultiplier-based PET/MRI system*, *Phys. Med. Biol.* **56** (2011) 4147.

[15] Y. Seiichi et al., *Simultaneous imaging using Si-PM-based PET and MRI for development of an integrated PET/MRI system*, *Phys. Med. Biol.* **57** (2012) N1.

[16] P.M. Duppenbecker et al., *Development of an MRI compatible digital SiPM based PET detector stack for simultaneous preclinical PET/MRI*, *IEEE Nucl. Sci. Symp. Med. Imag. Conf. Rec.* (2012) 3481.

[17] J. Wehner et al., *PET/MRI insert using digital SiPMs: Investigation of MR-compatibility*, *Nucl. Instrum. Meth.* **A 734 Part B** (2014) 116.

[18] J. Wehner et al., *MR-compatibility assessment of the first preclinical PET-MRI insert equipped with digital silicon photomultipliers*, *Phys. Med. Biol.* **60** (2015) 2231.

[19] B. Lee et al., *RF-Penetrable PET insert for simultaneous PET/MR imaging*, *EJNMMI Phys.* **1** (2014) 1.

[20] K.J. Hong et al., *A prototype MR insertable brain PET using tileable GAPD arrays*, *Med. Phys.* **40** (2013) 042503.

[21] H.G. Kang et al., *Initial results of SiPM-PET insert with short optical fiber bundles for simultaneous small animal PET/MR imaging*, *J. Nucl. Med.* **53** (2012) 489.

[22] S.J. Hong et al., *Concept Verification of Three-Layer DOI Detectors for Small Animal PET*, *IEEE Trans. Nucl. Sci.* **55** (2008) 912.

[23] G.B. Ko et al., *Development of a front-end analog circuit for multi-channel SiPM readout and performance verification for various PET detector designs*, *Nucl. Instrum. Meth.* **A 703** (2013) 38.

[24] P. Jezzard et al., *Correction for geometric distortion in echo planar images from B0 field variations*, *Magn. Reson. Med.* **34** (1995) 65.

[25] S. Witoszynskyj et al., *Phase unwrapping of MR images using Phi UN — a fast and robust region growing algorithm*, *Med. Imag. Anal.* **13** (2009) 257.

[26] H.F. Wehrl et al., *Assessment of MR compatibility of a PET insert developed for simultaneous multiparametric PET/MR imaging on an animal system operating at 7 T*, *Magn. Reson. Med.* **65** (2011) 269.

[27] F. Jiru et al., *Fast 3D radiofrequency field mapping using echo-planar imaging*, *Magn. Reson. Med.* **56** (2006) 1375.

[28] S. Akoka et al., *Radiofrequency map of an NMR coil by imaging*, *Magn. Reson. Imag.* **11** (1993) 437.

[29] G. Helms et al., *Rapid radiofrequency field mapping in vivo using single-shot STEAM MRI*, *Magn. Reson. Med.* **60** (2008) 739.

[30] L. Friedman et al., *Report on a multicenter fMRI quality assurance protocol*, *J. Magn. Reson. Imag.* **23** (2006) 827.

[31] R.E. Hendrick, *Breast MRI Fundamentals and Technical Aspects*, Springer, Berlin (2008).

[32] D. Stefan et al., *Quantitation of magnetic resonance spectroscopy signals: the jMRUI software package*, *Meas. Sci. Tech.* **20** (2009) 104035.

[33] D. Le Bihan et al., *Artifacts and pitfalls in diffusion MRI*, *J. Magn. Reson. Imag.* **24** (2006) 478.

[34] P.J. Basser et al., *Diffusion-tensor MRI: theory, experimental design and data analysis — a technical review*, *NMR Biomed.* **15** (2002) 456.

[35] G.C. Wiggins et al., *96-Channel receive-only head coil for 3 Tesla: design optimization and evaluation*, *Magn. Reson. Med.* **62** (2009) 754.

[36] B. Keil et al., *Massively parallel MRI detector arrays*, *J. Magn. Reson.* **229** (2013) 75.

[37] J. Wang et al., *Factors influencing flip angle mapping in MRI: RF pulse shape, slice-select gradients, off-resonance excitation, and B0 inhomogeneities*, *Magn. Reson. Med.* **56** (2006) 463.

[38] G.R. Morrell et al., *An analysis of the accuracy of magnetic resonance flip angle measurement methods*, *Phys. Med. Biol.* **55** (2010) 6157.

[39] E. Amaro Jr. et al., *Study design in fMRI: basic principles*, *Brain Cognit.* **60** (2006) 220.

[40] W.D. Heiss, *The potential of PET/MR for brain imaging*, *Eur. J. Nucl. Med. Mol. Imag.* **36 Suppl 1** (2009) S105.

[41] G. Krüger et al., *Neuroimaging at 1.5 T and 3.0 T: Comparison of oxygenation-sensitive magnetic resonance imaging*, *Magn. Reson. Med.* **45** (2001) 595.